JACS
JOURNAL OF THE AMERICAN CHEMICAL SOCIETY
Article
pubs.acs.org/JACS

Ultrafine NiO Nanosheets Stabilized by TiO_2 from Monolayer NiTi-LDH Precursors: An Active Water Oxidation Electrocatalyst

Yufei Zhao,[†] Xiaodan Jia,[†,‡] Guangbo Chen,[†,‡] Lu Shang,[†] Geoffrey I.N. Waterhouse,[§] Li-Zhu Wu,[†] Chen-Ho Tung,[†] Dermot O'Hare,[∥] and Tierui Zhang*[,†]

[†]Key Laboratory of Photochemical Conversion and Optoelectronic Materials, Technical Institute of Physics and Chemistry, Chinese Academy of Sciences, Beijing 100190, P. R. China

[‡]Key Laboratory of Synthetic and Natural Functional Molecule Chemistry of the Ministry of Education, College of Chemistry & Materials Science, Northwest University, Xi'an 710069, P. R. China

[§]School of Chemical Sciences, The University of Auckland, Auckland 1142, New Zealand

[∥]Chemistry Research Laboratory, Department of Chemistry, University of Oxford, Mansfield Road, Oxford OX1 3TA, United Kingdom

Supporting Information

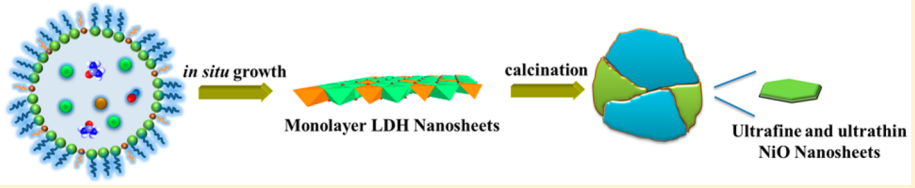

ABSTRACT: Faceted NiO nanoparticles preferentially exposing high surface energy planes demand attention due to their excellent electrocatalytic properties. However, the activity of faceted NiO nanoparticles generally remains suboptimal due to their large lateral size and thickness, which severely limits the availability of coordinatively unsaturated active reactive edge and corner sites. Here, ultrafine NiO nanosheets with a platelet size of ~4.0 nm and thickness (~1.1 nm) stabilized by TiO_2 were successfully prepared by calcination of a monolayer layered double hydroxide precursor. The ultrafine NiO nanosheets displayed outstanding performance in electrochemical water oxidation due to a high proportion of reactive NiO {110} facets, intrinsic Ni^{3+} and Ti^{3+} sites, and abundant interfaces, which act synergistically to promote H_2O adsorption and facilitate charge-transfer.

INTRODUCTION

NiO nanoparticles have attracted attention due to their widespread application in electrochemistry,[1−8] sensors, and catalysis.[9] Recently, faceted NiO nanoparticles exposing high surface energy planes have been the target of intense research focus due to their significantly enhanced catalytic performance.[10,11] However, the catalytic performance of these faceted NiO nanoparticles remains suboptimal due to their large lateral size and thickness leading to modest specific surface areas and limited exposure of the desired reactive facets. This has motivated the development of ultrathin two-dimensional (2D) nanomaterials, such as nanosheets, that preferentially expose a higher percentage of active sites.[12,13] However, most ultrathin 2D materials reported to date have lateral dimensions of several hundred nanometers, too large to dramatically improve catalytic performance due to the limited availability of edge and corner sites which possess high reactivity due to coordinative unsaturation. Synthesis methods that can yield both ultrafine and ultrathin NiO nanosheets are demanded.[14,15] The surface energy of NiO facets follows the order {110} ≈ {101} > {113} > {100}.[16] Since surface chemical reactivity generally increases with surface energy,[17] it is highly desirable to synthesize ultrafine NiO nanosheets (diameter < 10 nm, thickness ~1 nm) exposing a high proportion {110}-facets to achieve more efficient catalytic performance.

Currently, there is enormous interest in the development of electrocatalysts for water splitting, motivated by increasing global energy demand and the need to develop sustainable energy technologies for future generations.[18] Water splitting requires efficient electrocatalysts for the oxygen evolution reaction (OER) and the hydrogen evolution reaction (HER).[19] According to Yang's pioneering work,[20] 3d transition-metal-based electrocatalysts with a surface cation e_g orbital occupancy approaching unity, such as Ni^{3+} ($t_{2g}^6e_g^1$), represent the most ideal candidates for OER catalysts due to the increased covalency of transition metal−oxygen bonds in such systems.[21] Hexagonal bulk NiO has a $t_{2g}^6e_g^2$ electronic configuration. However, the high abundance of surface defects (nickel vacancies) presented in ultrathin NiO nanosheets is expected to significantly alter the electronic structure of Ni^{2+} centers, producing Ni^{3+} sites ($t_{2g}^6e_g^1$). A very high OER activity is therefore anticipated in ultrafine and ultrathin NiO nanosheet sytems having highly exposed {110}

Received: February 12, 2016
Published: May 9, 2016

DOI: 10.1021/jacs.6b01606
J. Am. Chem. Soc. 2016, 138, 6517−6524

reactive planes and Ni cations with the desired $t_{2g}^6e_g^1$ electronic configuration.[22]

Heterostructured catalysts with abundant interfaces that facilitate charge separation have attracted much attention in photo/electrocatalysis for solar fuels and chemicals,[23−26] which motivated us to distribute NiO within an inorganic matrix to both control NiO morphology and improve charge separation and electrocatalytic performance. Layered double hydroxides (LDHs) are a family of 2D layered clays and have been widely studied as catalyst supports or precursors due to the tunability of their composition and morphologies.[27−30] Calcination of LDH nanosheets yields mixed metal oxide (MMO) nanosheets through a topotactic transformation.[31] By calcination of a nanosized ultrathin NiTi-LDH nanosheet precursor, we postulated that it should be possible to obtain ultrathin NiO nanosheets exposing reactive NiO {110} facets and controllable size, due to the stabilizing influence of TiO_2 also formed during the calcination step.

In this paper, we describe the successful fabrication of ultrafine and ultrathin NiO nanosheets (size ∼4 nm, thickness ∼1 nm) stabilized by TiO_2 by calcination of monolayer thick NiTi-LDH nanosheets synthesized using a reverse microemulsion method (Scheme 1). The NiO/TiO_2 heterostructures exhibit very high

Scheme 1. Schematic Illustration of the Synthesis of Ultrafine and Ultrathin NiO Nanosheets Stabilized by TiO_2 from Monolayer NiTi-LDH Nanosheet Precursors

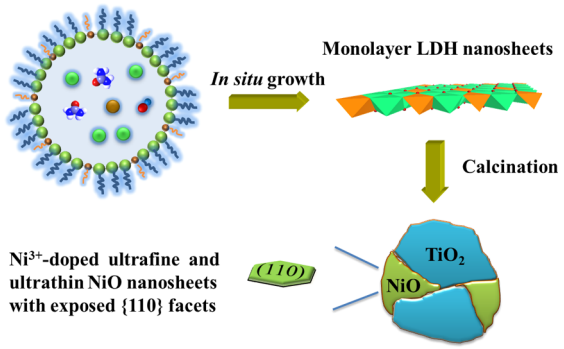

OER activity in water, which originates from the high proportion of exposed NiO-{110} facets, coordinatively unsaturated surface Ni^{3+} and Ti^{3+} active sites, and abundant NiO/TiO_2 heterojunctions which facilitate charge-transfer and enhance H_2O adsorption.

RESULTS AND DISCUSSION

The monolayer NiTi-LDH nanosheets synthesized by the reverse microemulsion method exhibited a uniform plate-like shape with mean platelet diameter ∼20 nm and mean thickness 0.8 ± 0.1 nm (Figure 1A, Figure S1). The thickness of the NiTi-LDH nanosheet was nearly identical to that reported for monolayer MgAl-LDH nanosheets.[32] Thermal gravimetric analysis results revealed the decomposition of surface adsorbed species and hydroxide layers, as well as the formation of oxides and spinel. After calcination at 500 °C, the monolayer NiTi-LDH nanosheets were transformed into NiTi mixed metal oxide nanosheets (denoted as Mono-NiTi-MMO). Calcination at a higher temperatures (e.g., 800 °C) was undesirable, resulting in the spinel phase ($NiTiO_3$) becoming the main product (Figure S2).[33] XRD studies of Mono-NiTi-MMO confirmed the coexistence of anatase TiO_2 and cubic NiO, with the characteristic Bragg reflections for each oxide being significantly broader and weaker than those seen for a bulk NiTi-MMO (Bulk-NiTi-MMO) reference sample prepared by a conventional coprecipitation route followed by calcination at 500 °C (Figure S3A). The line broadening observed in the XRD for Mono-NiTi-MMO is attributed to the very small particle size and low crystallinity. The lateral sizes of the NiO and TiO_2 particles were calculated to be ∼4.0 and 11.0 nm, respectively, using the Scherrer equation (Table S1). Transmission electron microscope (TEM) analyses revealed the particle size of Mono-NiTi-MMO to be ∼20 nm, which was comparable to its LDH precursor (Figure 1B). Figure 1C shows a typical high-resolution TEM (HRTEM) image for Mono-NiTi-MMO, and displays lattice fringes with spacings of 0.24, 0.21, and 0.19 nm that are indexed to the (111) and (200) facets of NiO nanosheets, and the (200) facet of anatase TiO_2, respectively. An interfacial angle of ∼55.0° was determined between the NiO (111) and (200) facets. The corresponding fast Fourier transform (FFT) pattern (Figure 1D) further confirmed the existence of (111) and (200) lattice planes. The HRTEM analysis revealed that the geometry of the NiO was likely hexagonal with dominant (110) facets (Figure 1E).[11] The NiO nanosheets were determined by TEM to have a mean particle size of ∼4 nm, which agrees with the XRD result. Further, the NiO nanosheets were highly dispersed by TiO_2, which is advantageous in mitigating the undesirable aggregation of the NiO nanosheets. Further, the heterojunctions formed between the NiO nanosheets and TiO_2 were expected to alter the geometric/electronic structure of NiO, an aspect we explore in detail below. The anatase TiO_2 nanosheets in Mono-NiTi-MMO mainly exposed (001) facets (Figure S4).[34] The highly exposed NiO (110) and TiO_2 (001) facets in Mono-NiTi-MMO, together with an excellent lattice match (Figure S5), reflect the topological transformation of the hexagonal structured LDH nanosheets during calcination.[35] In the absence of titanium cations in the LDH precursor, the obtained ultrathin NiO nanosheets (denoted as NS-NiO) similarly exposed (110) facets but exhibited a larger particle size (∼20 nm) and thickness (∼2.0 nm) as shown in Figure S6. The presence of titanium cations during the calcination step is thus important for controlling the particle size and thickness of NiO nanosheets. The chemical composition of Mono-NiTi-MMO was also determined to be 1.6:1 for Ni/Ti (Figure S7). The thickness of Mono-NiTi-MMO was determined by atomic force microscopy (AFM) to be ∼1.1 ± 0.1 nm (Figure 1F,G), which agrees well with the 1.1 nm thickness of a 5-atom-thick NiO slab along the [110] direction. The increased thickness of Mono-NiTi-MMO compared to that of the corresponding LDH precursor (∼0.8 ± 0.1 nm) is due to the structure evolution of the LDH during calcination.[35] Bulk-NiTi-MMO exhibited a considerably larger particle size (∼100 nm) and thickness (∼13 nm) (Figure S8), and the commercial NiO reference sample had a lateral size of ∼25 nm (Figure S9). As expected for a material with almost atomic thickness, Mono-NiTi-MMO possessed a higher specific surface area (165.8 $m^2\ g^{-1}$) compared with those of NS-NiO (127.9 $m^2\ g^{-1}$), Bulk-NiTi-MMO (98.1 $m^2\ g^{-1}$), and NiO (147.1 $m^2\ g^{-1}$) (Figure S3B). The ultrafine and ultrathin morphology of the NiO nanosheets in Mono-NiTi-MMO could potentially expose more chemically reactive low coordinated Ni cations than NS-NiO or Bulk-NiTi-MMO,[36] thereby affording superior electrocatalytic activity, an aspect we explore in detail below.

X-ray absorption near-edge structure (XANES) spectroscopy was used to probe the local atomic structure of Ni in commercial NiO, Bulk-NiTi-MMO, and Mono-NiTi-MMO. As shown in

DOI: 10.1021/jacs.6b01606
J. Am. Chem. Soc. 2016, 138, 6517−6524

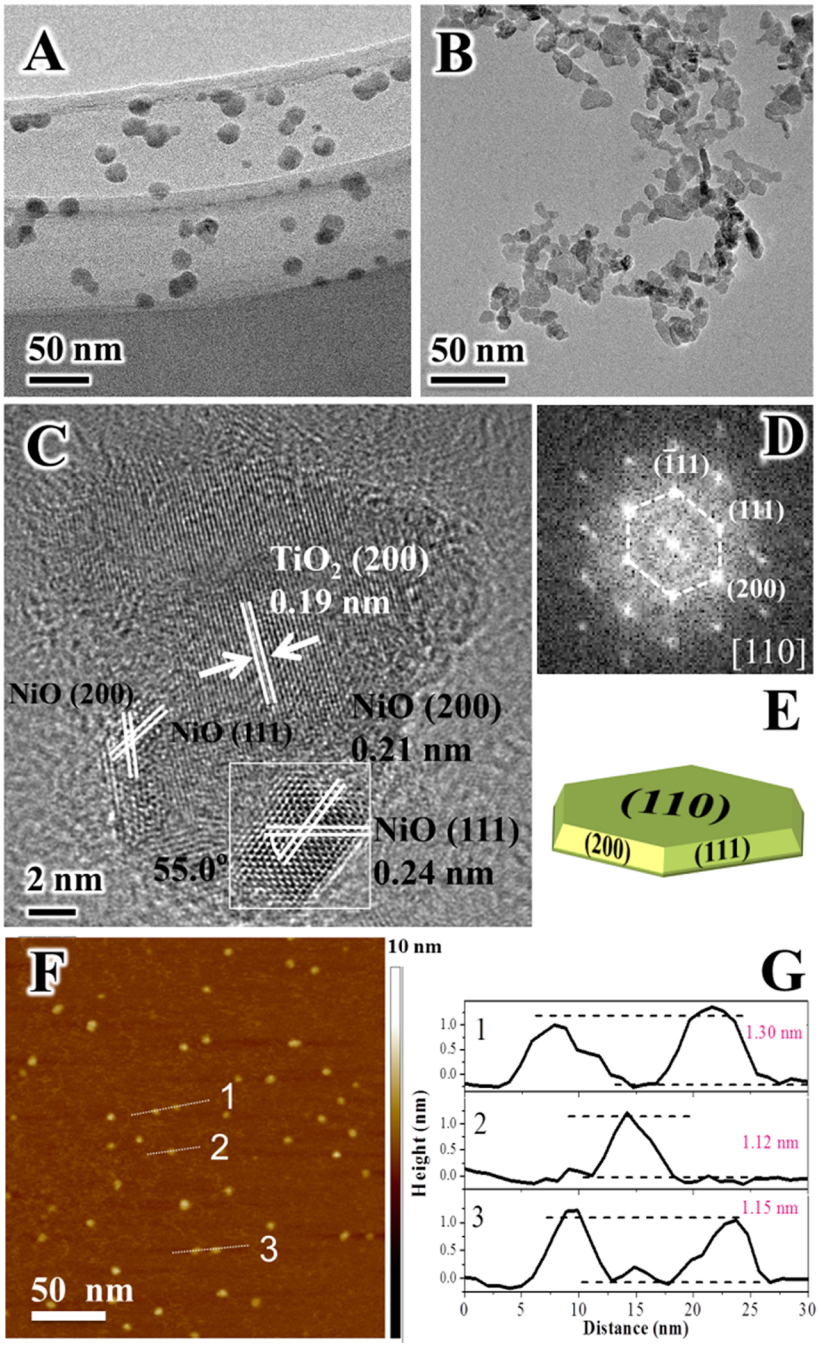

Figure 1. (A) TEM image of monolayer NiTi-LDH nanosheets, (B, C) TEM and HRTEM images of Mono-NiTi-MMO, (D) FFT pattern of the corresponding NiO area, (E) geometrical model of the hexagonal NiO nanocrystal, (F) AFM image, and (G) the corresponding height profiles of Mono-NiTi-MMO. The numbers from 1 to 3 in part G correspond to the line scan numbers in part F.

Figure 2A,B, the Ni K-edge XANES spectra and the corresponding *k*-space spectra of Bulk-NiTi-MMO and Mono-NiTi-MMO are similar, and closely resemble that of the NiO reference, except in the case of Mono-NiTi-MMO where the absorption edge was shifted to higher energies (Figure 2A, inset) and showed fewer oscillations, indicating a higher average Ni oxidation state and structural differences in the coordination environment surrounding the Ni atoms, respectively (Figure 2B). From the R space plot for Mono-NiTi-MMO (Figure 2C), it was determined that the first Ni−O shell has a distance of ∼2.05 Å and coordination number (*N*) of 5.70 (Table S2), which is assigned to the Ni−O octahedra. The Ni−O distance of ∼2.05 Å is smaller than those of 2.08 Å observed for both NiO and Bulk-NiTi-MMO. Furthermore, in the Ni−Ni shell, the *N* for Mono-NiTi-MMO was only 7.70 compared to 12.00 for both NiO and Bulk-NiTi-MMO, indicating the existence of nickel vacancies (V_{Ni}) in Mono-NiTi-MMO.[37] The average Ni−Ni distance of ∼2.98 Å for Mono-NiTi-MMO is slightly larger than that of the other samples (2.96 Å). In addition, the larger Debye−Waller factors of Mono-NiTi-MMO also indicate more structural distortion about Ni centers in Mono-NiTi-MMO. This situation is depicted schematically in Figure 2D, where the six nearest O atoms move away from V_{Ni} by 0.03 Å (the movement of four in-plane oxygen atoms is shown), significantly decreasing the average distance of neighboring Ni atoms with O atoms. Meanwhile, neighboring Ni atoms move slightly closer to V_{Ni},

DOI: 10.1021/jacs.6b01606
J. Am. Chem. Soc. 2016, 138, 6517−6524

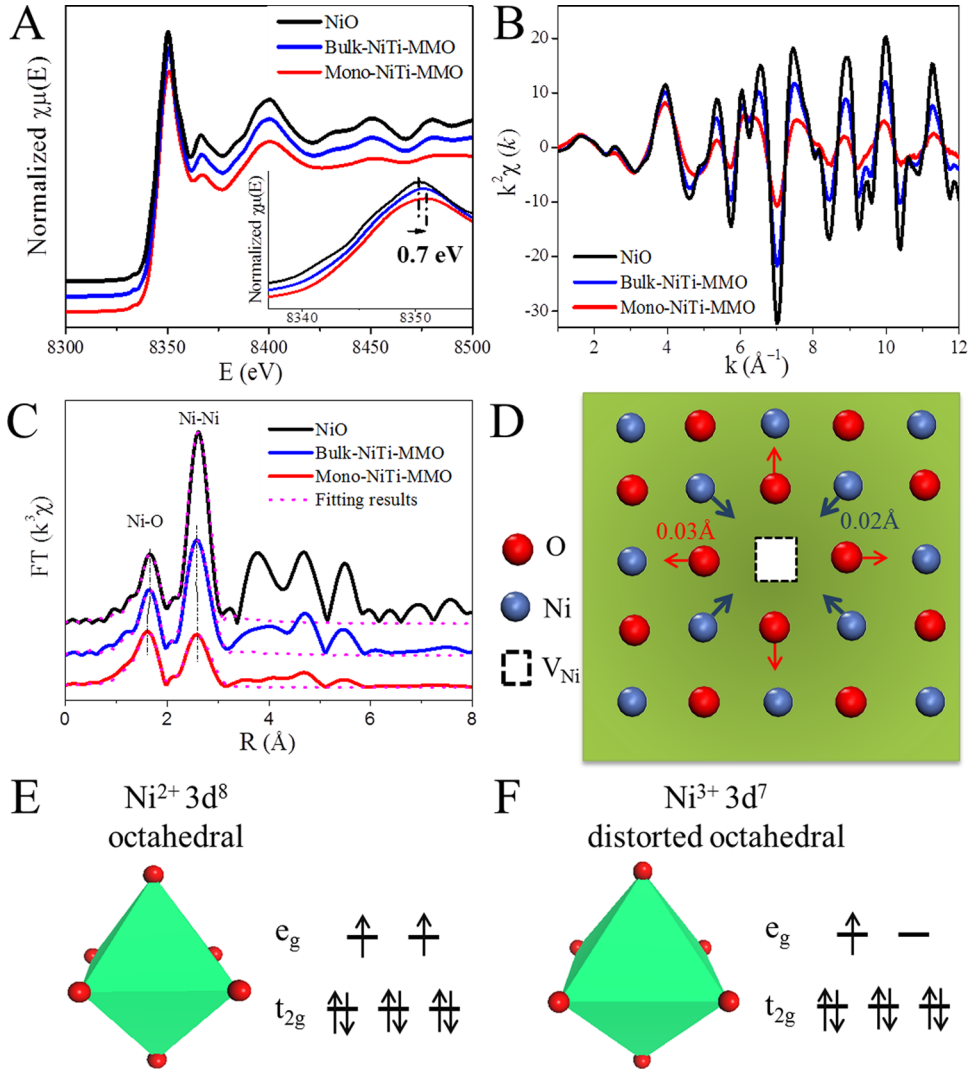

Figure 2. (A) Ni K-edge XANES spectra; (B) Ni K-edge extended XANES oscillation functions $k^2\chi$ (k); and (C) magnitude of k^2-weighted Fourier transforms of the Ni K-edge XANES spectra for NiO, Bulk-NiTi-MMO, and Mono-NiTi-MMO with corresponding curve-fitting results; and (D) schematic view of the Ni and O atoms relaxation around V_{Ni} in Mono-NiTi-MMO. O atoms move outward, and Ni atoms move inward to V_{Ni}. Schematic electronic configuration of the Ni cations in NiO_6 of (E) bulk NiO and (F) V_{Ni} doped NiO.

leading to an increased average Ni−Ni distance. Thus, the octahedral distortions observed by EXAFS for Mono-NiTi-MMO can be rationalized in terms of the existence of V_{Ni} in the NiO nanosheets resulting from size reduction effects.[38] Ti K-edge XANES spectra (Figure S10) reveal that the distance of the first Ti−O shell in Mono-NiTi-MMO is smaller than that in Bulk-NiTi-MMO, evidence that the TiO_6 octahedral distortions are also present in Mono-NiTi-MMO.

Electron spin resonance (ESR) was also used to probe the valence states of Ni and Ti in Bulk-NiTi-MMO and Mono-NiTi-MMO. ESR signals with g = 2.172 were ascribed to Ni^{3+} species, and g = 1.996 signals assigned to Ti^{3+} species were found for Mono-NiTi-MMO, whereas Bulk-NiTi-MMO was ESR-silent (Figure S11A).[39,40] Fominykh and co-workers reported that, on decreasing the particle size of NiO to the nanoscale, surface Ni^{2+} atoms are partially oxidized to Ni^{3+} due to atomic-scale defects.[1] The presence of metallic defects in Mono-NiTi-MMO was further confirmed by X-ray photoelectron spectroscopy (XPS). For Bulk-NiTi-MMO, a $2p_{3/2}$ peak at 458.8 eV and characteristic for Ti^{4+} was observed. For Mono-NiTi-MMO, an additional $2p_{3/2}$ peak at 458.2 eV is observed and assigned to Ti^{3+} species, consistent with the ESR results above. Figure S11C shows Ni 2p XPS spectra for NiO and Bulk-NiTi-MMO, which comprise peaks at 853.4 and 870.8 eV in a 2:1 area ratio which are readily assigned to the $2p_{3/2}$ and $2p_{1/2}$ signals, respectively, of Ni^{2+} in NiO. Characteristic Ni^{2+} "shake up" satellites are also seen on the high binding energy side of the main Ni 2p peaks. The Ni 2p XPS spectra for Mono-NiTi-MMO and NS-NiO show a much weaker Ni^{2+} contribution, and are instead dominated by signals due to Ni^{3+} which are located at higher binding energies (855.3 and 872.7 eV, respectively). Ni^{3+} also shows displays characteristic "shake up" satellites. The predominance of Ni^{3+} and Ti^{3+} in Mono-NiTi-MMO results from V_{Ni} and oxygen vacancies (V_O) created during the calcination step used for the formation of the ultrafine NiO and TiO_2 nanosheets. In order to achieve charge neutrality near the formed nickel and oxygen vacancies, surface Ni^{2+} is oxidized to Ni^{3+},[41] and Ti^{3+} is created near V_O. TiO_2 may draw electrons from NiO, leading to the increased oxidation state of Ni near NiO/TiO_2 heterojunctions. The unique electronic structure of Mono-NiTi-MMO with the predominance of Ni^{3+} and Ti^{3+} defects was expected to impart high electrical

DOI: 10.1021/jacs.6b01606
J. Am. Chem. Soc. 2016, 138, 6517−6524

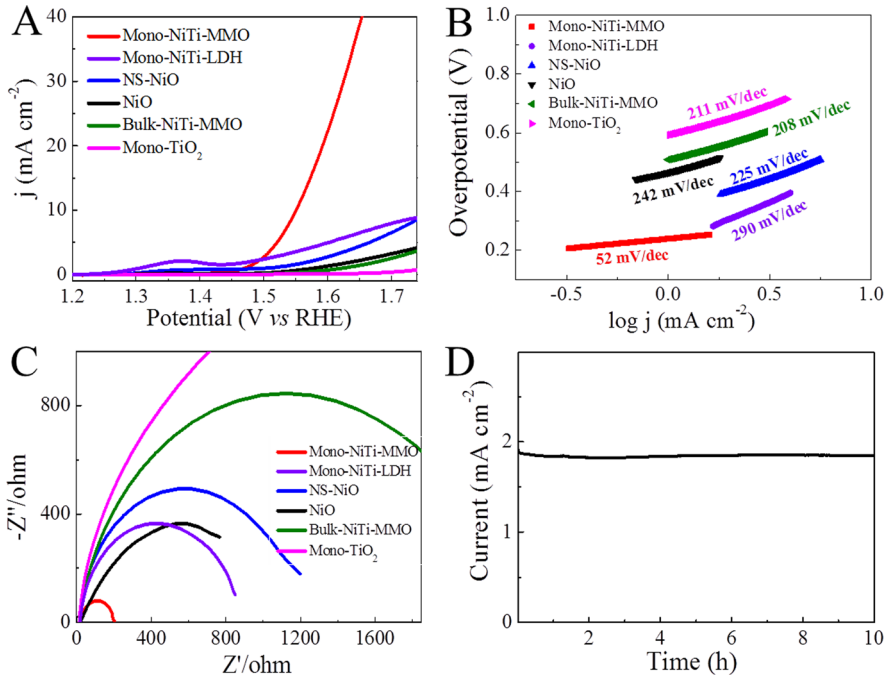

Figure 3. OER performance: (A) linear sweep voltammetry (LSV) curves; (B) corresponding Tafel plots; (C) electrochemical impedance spectra for Mono-NiTi-MMO, Mono-NiTi-LDH, NS-NiO, NiO, Bulk-NiTi-MMO, and Mono-TiO_2; (D) durability test for Mono-NiTi-MMO over 10 h.

conductivity and facilitate efficient charge-transfer during electrochemical water splitting, and is explored in detail below.

As mentioned earlier, the occupancy of e_g orbitals in 3d transition-metal-based electrocatalysts determines the metal−oxygen bond strength, and strongly influences the overpotential of OER. Electrocatalysts with too low or too high e_g occupancy (0 or 2, respectively) bind oxygen too weakly or too strongly, respectively, leading to poor water splitting performance.[20,42,43] Xie et al. recently reported that Co_3S_4 and $CoSe_2$ nanosheets exhibit excellent electrocatalytic water splitting performance through optimizing e_g filling and the fraction of exposed polyhedra in the nanosheets.[22,44] Compared with a $t_{2g}^6e_g^2$ electronic configuration of Ni^{2+} in bulk NiO (Figure 2E), Ni^{3+} active sites in distorted NiO nanosheets possess a near-unity occupancy of the e_g orbital ($t_{2g}^6e_g^1$) (Figure 2F), which is optimal for efficient OER performance.[20] Besides the Ni defects, the oxygen vacancies are important defects for improving the photo/electrochemical performance in metal oxide systems (i.e., TiO_2 and ZnO).[45,46] Recent investigations demonstrate that the oxygen vacancies (Ti^{3+} active sites) improve the donor densities, thereby enhancing the electrical conductivity and charge-transport properties of TiO_2-based catalysts. Furthermore, oxygen vacancies serve as adsorption and active sites, facilitating charge-transfer at the electrode/electrolyte interface and improving performance of oxide systems in supercapacitors,[45] batteries,[47] and photoelectrochemical water splitting.[48,49]

The highly exposed reactive NiO {110} facets in Mono-NiTi-MMO, along with the presence of Ni^{3+} with highly active e_g orbitals and the abundant interfaces as well as the existence of Ti^{3+} active sites, were all expected to enhance the OER activity of Mono-NiTi-MMO.[50] Water oxidation experiments conducted in 1.0 M KOH showed that the Mono-NiTi-MMO electrocatalyst afforded a current density up to 10 mA m^{-2} at 1.55 V versus RHE at an overpotential (η) of 0.32 V, roughly 3, 6, 15, and 34 times larger than that of Mono-LDH-LDH, NS-NiO, NiO, and Bulk-NiTi-MMO, respectively, confirming the excellent water oxidation activity of Mono-NiTi-MMO (Figure 3A). For Mono-LDH-LDH, the first peak around 1.38 V versus RHE is attributed to the characteristic interconversion of Ni^{2+}/Ni^{3+} mediated by OH^-.[51] The Tafel plot for Mono-NiTi-MMO gave a value of 52 mV/decade (Figure 3B), which was much smaller than that determined for Mono-NiTi-LDH, NS-NiO, Bulk-NiTi-MMO, and NiO. A low Tafel plot value indicates a superior OER ability with decreasing overpotential. To further access information about the active sites in the above samples for the OER, it was assumed that the Ni sites were catalytically active, and their turnover frequencies (TOFs) were calculated (Figure S12A). Mono-NiTi-MMO showed a much higher TOF (0.068 s^{-1}) at an overpotential of 0.50 V, which was approximately 8, 14, 34, and 24 times higher than the corresponding values determined for Mono-NiTi-LDH (0.009 s^{-1}), NS-NiO (0.005 s^{-1}), NiO (0.002 s^{-1}), and Bulk-NiTi-MMO (0.003 s^{-1}), respectively. The excellent electrochemical activity of Mono-NiTi-MMO can thus be understood in terms of significantly decreased charge-transfer resistance due to the high concentration of V_{Ni} compared to Mono-NiTi-LDH, NS-NiO, NiO, or Bulk-NiTi-MMO (Figure 3C). Moreover, Mono-NiTi-MMO gives about ∼100% Faradaic yield, indicating the O_2 evolution was driven by Mono-NiTi-MMO electrocatalysts (Figure S12B). TiO_2 nanosheets with Ti^{3+} sites (denoted as Mono-TiO_2, Figure 3A,B and Figure S13), obtained by acid treatment of Mono-NiTi-MMO, did not exhibit any obvious OER activity, indicating that Ti^{3+} sites in TiO_2 are not OER active. Conversely, Ti^{3+} sites in Mono-NiTi-MMO act as cocatalysts in OER by improving the electrical conductivity, the charge-transport between NiO and TiO_2 nanosheets, as well as the charge-transfer efficiency at the catalysts/electrolyte interfaces. Evidence for improved electrical conductivity is seen by the decreased resistance compared to defect-free TiO_2 nanoparticles (Figure S14). Table S4 summarizes the OER activities of some widely used NiO-based electrocatalysts. The data indicate that Mono-NiTi-MMO containing ultrafine NiO nanosheets shows superior activity to

DOI: 10.1021/jacs.6b01606
J. Am. Chem. Soc. 2016, 138, 6517−6524

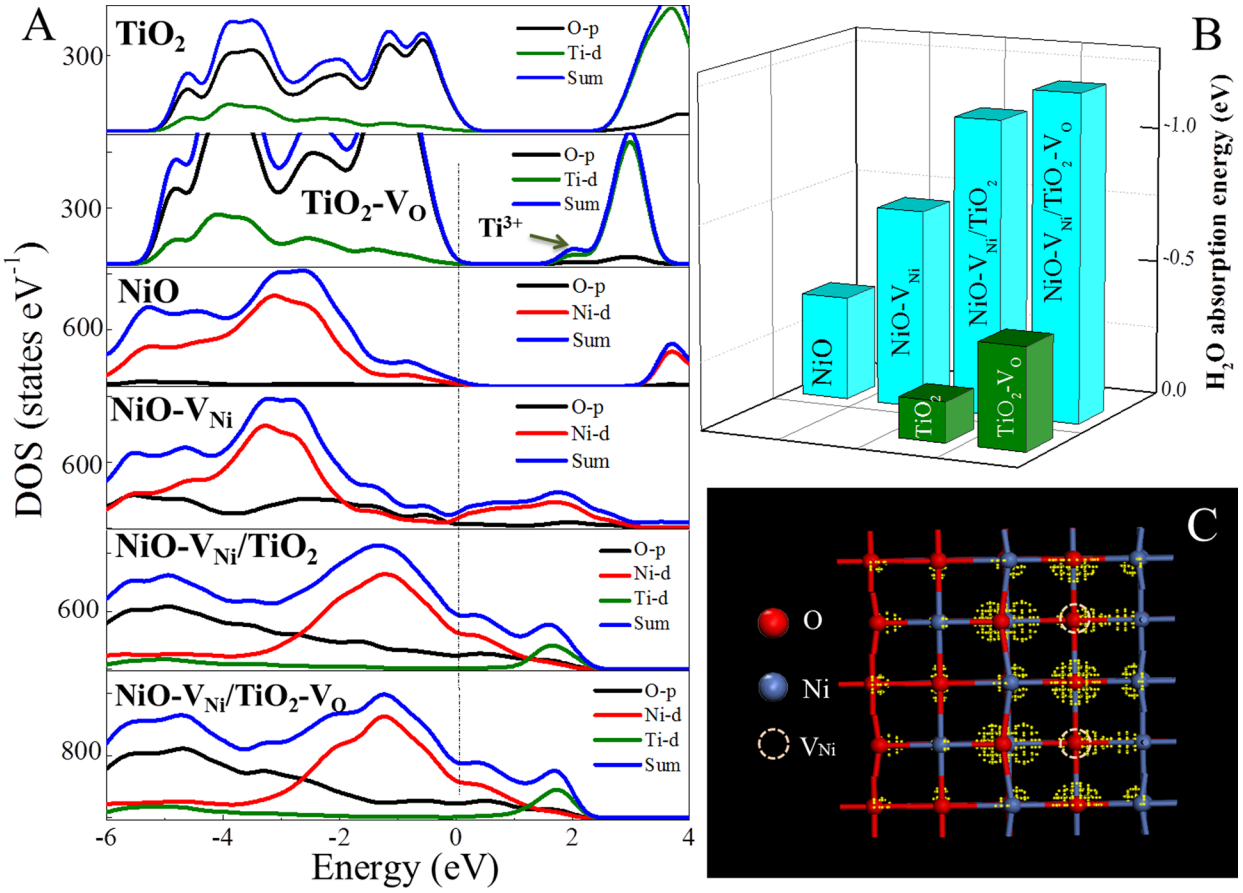

Figure 4. (A) TDOS and PDOS (the Fermi energy level E_F was set to zero); (B) DFT-calculated adsorption energies of H_2O molecules on the surfaces of TiO_2, TiO_2-V_O, NiO, NiO-V_{Ni}, NiO-V_{Ni}/TiO_2, and NiO-V_{Ni}/TiO_2-V_O; and (C) charge density distribution for the valence band maximum of NiO-V_{Ni}.

most reported Ni-based oxide electrocatalysts for OER. To evaluate the durability of Mono-NiTi-MMO for water oxidation in an alkaline electrolyte, continuous OER at static current was performed. Figure 3D revealed that Mono-NiTi-MMO retained its electrocatalytic activity over the 10 h test period. Furthermore, the morphology of Mono-NiTi-MMO after OER was almost identical to that before reaction (Figure S15), suggesting that the NiO nanosheets with highly exposed {110} reactive facets in Mono-NiTi-MMO were very stable against aggregation during OER due to physical separation by the TiO_2 nanosheets.

Density functional theory (DFT) calculations were used to examine the total densities of states (TDOS) as well as the partial densities of states (PDOS) for TiO_2, NiO systems with and without V_O and V_{Ni}, respectively, and NiO/TiO_2 heterostructure (Figure 4, Figure S16). As shown in Figure 4A, compared with the pure TiO_2 and NiO system with an obvious bandgap, the DOS of V_{Ni}-doped NiO (denoted as NiO-V_{Ni}) and NiO-V_{Ni}/TiO_2 around the Fermi level are continuous without any gap, while V_O-doped TiO_2 (denoted as TiO_2-V_O) has a narrow bandgap with the bottom of the conductive band dominated by Ti^{3+}, in accordance with Liu's results.[52] These results confirm that NiO-V_{Ni} and NiO-V_{Ni}/TiO_2 are more metal-like with good charge-transfer efficiencies, and that charges in TiO_2-V_O systems with reduced bandgaps can more easily transfer compared with bulk TiO_2 without Ti^{3+} defects. Moreover, the remarkably increased DOS near the Fermi level of NiO-V_{Ni}/TiO_2-V_O with the introduction of V_{Ni} and V_O accounts for the high carrier concentration and high electrical conductivity determined experimentally for Mono-NiTi-MMO. The minor differences in the DOS values between NiO-V_{Ni}/TiO_2-V_O and NiO-V_{Ni}/TiO_2 can be rationalized in terms of severe structural disorder on the surface of these electrocatalysts. The ability of electrocatalysts to absorb H_2O generally affects the water oxidation activity.[44,53] Figure S16 reveals the optimized adsorption structure and the binding energy (E_b) of H_2O on defect-free NiO, NiO-V_{Ni}, NiO-V_{Ni}/TiO_2, and NiO-V_{Ni}/TiO_2-V_O. NiO-V_{Ni} has an adsorption energy (absolute datum) for H_2O of 0.73 eV, which is significantly larger than that of H_2O on defect-free NiO (0.38 eV). After the formation of heterostructured NiO-V_{Ni}/TiO_2 by adding TiO_2 nanosheets, the adsorption energy of H_2O increased significantly (1.09 eV). Introducing V_O in the NiO-V_{Ni}/TiO_2 heterostructure increased structural disorder on the surface, resulting in an even higher value for the adsorption of H_2O (1.21 eV) (Figure 4B). These results indicate that V_{Ni} in NiO promotes the adsorption of H_2O, with abundant interfaces of NiO/TiO_2 increasing the charged density (Figure S17) and further contributing to the adsorption of H_2O, all of which enhances the water oxidation kinetics. Moreover, the Ti^{3+} sites further increase the adsorption energy of H_2O on the catalysts, and also increase charge-transport from the surface of catalysts to H_2O. The charge distribution of the orbital wave function at the valence band maximum of NiO-V_{Ni} shows that the charge density of the defective NiO mainly concentrates at the O atoms near V_{Ni} (Figure 4C). A similar result was also found in TiO_2-V_O systems (Figure S18), indicating the increased donor density of V_O-containing TiO_2, and further facilitating the charge-transport,

DOI: 10.1021/jacs.6b01606
J. Am. Chem. Soc. 2016, 138, 6517−6524

which aligns well with the EIS results (Figure S14). Tanaka and co-workers reported that Ti^{3+} defects in TiO_2 improve the electrical conductivity owing to the increased donor density (electron density) and promoting the efficiency of photoelectrochemical water oxidation.[54] Results reveal that valence electrons in the defective NiO and TiO_2 systems are able to travel more freely than in the defect-free NiO and TiO_2 systems, a result well-supported by the electrochemical impedance spectroscopy result in Figure 3C. The high electron mobility in Mono-NiTi-MMO contributes to its remarkable water oxidation performance.

Results here confirm the excellent potential of Mono-NiTi-MMO heterostructure as an OER electrocatalyst. The superior water oxidation performance can be explained as follows: (1) The highly exposed {110} reactive facets in ultrafine NiO provide numerous active sites for OER. (2) The abundant Ni^{3+} surface active sites with unity occupancy of the e_g orbital ($t_{2g}^6e_g^1$), and the local structural distortions about V_{Ni}, help facilitate electron transfer. (3) The existence of Ti^{3+} generated by V_O in TiO_2 nanosheets further facilitates charge-transport by increasing the donor density, and also improves charge-transfer efficiency at the catalysts/electrolyte interface by providing coordinative unsaturated site for efficient water adsorption. (4) From the Lewis acid−base concept, the electron donation from the NiO nanosheets to TiO_2 nanosheets around the heterostructure interfaces makes the NiO nanosheets more acidic, promoting the adsorption of OH^-, leading to improved OER activity.

CONCLUSION

In summary, ultrafine NiO nanosheets with a particle diameter of ∼4.0 nm and thickness of ∼1.1 nm stabilized by TiO_2 have been obtained by calcination of monolayer NiTi-LDH nanosheets. The Mono-NiTi-MMO heterostructure demonstrates outstanding performance for OER. TEM, EXAFS, ESR, and DFT calculations established that the atomic-thick NiO nanosheets in Mono-NiTi-MMO expose a high percentage of reactive {110} facets containing Ni^{3+} active sites, abundant interfaces, as well as Ti^{3+} sites, with the latter improving charge-transfer/transport efficiency and thereby promoting H_2O adsorption, resulting in the significantly improved H_2O oxidation activity. This work demonstrates the potential of novel ultrafine and ultrathin oxides materials for electrocatalytic applications. Using this same synthetic strategy, other metallic oxide nanosheet electrocatalysts with controllable exposed high-energy facets and desirable e_g orbital occupancy, such as FeO_x, CoO_x, MnO_x, could be obtained.

EXPERIMENTAL SECTION

Synthesis of Monolayer NiTi-LDH Nanosheets. Monolayer NiTi-LDH nanosheets were synthesized using a reverse microemulsion method.[29] Typically, 1.1 mL of water, 50 mL of isooctane, and 1.80 g of SDS were mixed to form a transparent reverse emulsion system with the assistance of the cosurfactant 1-butanol (1.5 mL). Then, 0.004 mol of $Ni(NO_3)_2{\cdot}6H_2O$, 0.001 mol of $TiCl_4$, and 1.2 g of urea were added, and the resulting mixture was aged at 110 °C for 27 h in an oil bath. Finally, the precipitates were washed several times.[32] For comparison, bulk NiTi-LDH was also prepared according to a literature method.[55]

Synthesis of NiTi MMO. NiTi MMO nanosheets were synthesized by calcining monolayer NiTi-LDH nanosheets at 500 °C for 2 h with a heating rate of 5 °C min^{-1}. The bulk NiTi-MMO was obtained by calcining the bulk NiTi-LDH precursor under that same reaction conditions used to prepare the NiTi MMO nanosheets.

The synthesis of ultrathin NiO nanosheets was similar to that used to synthesize NiTi MMO nanosheets, except that $TiCl_4$ was not added as a reagent.

Characterization. X-ray diffraction (XRD) patterns were collected using a Bruker DAVINCI D8 ADVANCE diffractometer. Sample morphologies were characterized using a JEOL-TEM and Hitachi S-4800 field emission scanning electron (SEM) microscope with quantitative X-ray spectroscopy (EDX) capabilities. The size and thickness of oxide nanosheets were determined by AFM (Multimode Nanoscope IIIa, Veeco Instruments). Thermogravimetry analysis (TGA) was carried out on a PCT-1A thermal analysis system under ambient atmosphere with a heating rate of 10 °C min^{-1}. Brunauer−Emmett−Teller (BET) surface areas and pore-size distributions were determined by N_2 physisorption at 77 K using a Quantachrome Autosorb-1C-VP apparatus. XPS spectra were carried out on a PHIQ2000 X-ray photoelectron spectrometer, and calibrated against the C 1s peak at 284.8 eV of adventitious hydrocarbons. ESR spectra were collected on a JES-FA200 at 110 K in an Ar atmosphere. Ni and Ti K-edge XANES measurements were performed at the 1W1B beamline of Beijing Synchrotron Radiation Facility. The O_2 amount was detected by gas chromatography (GC) analysis (Shimadzu GC-2014C) with a thermal conductivity detector (TCD).

Electrochemical Tests. The electrochemical measurements were performed on a CHI 660B electrochemical workstation with a three-electrode cell, comprising a platinum foil counter electrode, a saturated Hg/HgO reference electrode, and a glassy carbon working electrode coated with electrocatalysts. The linear sweep voltammetry curves were recorded a scan rate of 5 mV s^{-1} in deaerated acetonitrile with KOH (1 mol L^{-1}) as the electrolyte. The electrochemical impedance spectroscopy (EIS) measurements were conducted over a frequency range 1−10^5 Hz. For the measurements, electrocatalysts (5 mg) and Nafion solution (30 μL, 5 wt %) were added to 1 mL of aqueous ethanol (25 vol % EtOH), followed by sonication to achieve good electrocatalyst dispersion. Then, 5 μL of the resulting dispersion was deposited onto a glassy carbon electrode (3 mm diameter with an electrocatalyst loading of ∼0.34 mg cm^{-2}). TOFs were calculated as the number of O_2 molecules evolved per site per second.[56] The active Ni was calculated as the only active site in Mono-NiTi-MMO. The Faradaic efficiency of OER catalysts is defined as the ratio of the amount of experimentally tested O_2 to that of the theoretically expected O_2 from the OER reaction. The theoretically expected amount of O_2 was then calculated by applying the Faraday law, which states that the passage of 96 485.4 C causes 1 equiv of reaction.

DFT Calculations. Plane-wave DFT + U calculations of the electronic properties of NiO systems with exposed {110} facets and Ni^{3+} doped NiO with Ni defect sites, TiO_2 systems with exposed {001} facets and Ti^{3+} doped TiO_2 with O defect sites, and NiO-V_{Ni}/TiO_2 heterostructure with and without V_O were carried out using CASTEP module in Material Studio. The calculation details were the same as those reported in our previous paper.[57]

ASSOCIATED CONTENT

Supporting Information

The Supporting Information is available free of charge on the ACS Publications website at DOI: 10.1021/jacs.6b01606.

Extended characterization results, including TEM, TGA, BET, ESR, and XPS data, electrochemical data, and DFT results (PDF)

AUTHOR INFORMATION

Corresponding Author

*tierui@mail.ipc.ac.cn

Notes

The authors declare no competing financial interest.

DOI: 10.1021/jacs.6b01606
J. Am. Chem. Soc. 2016, 138, 6517−6524

■ ACKNOWLEDGMENTS

The authors are grateful for the financial support from the Ministry of Science and Technology of China (2014CB239402, 2013CB834505), the Key Research Programme of the Chinese Academy of Sciences (KGZD-EW-T05), the National Natural Science Foundation of China (21401206, 51322213, 51172245, 51572270, 21301183, 21401207), the Beijing Natural Science Foundation (2152033, 2154058), and the National Program for Support of Top-notch Young Professionals. The XAFS experiments were conducted in 1W1B beamline of Beijing Synchrotron Radiation Facility (BSRF).

■ REFERENCES

(1) Fominykh, K.; Feckl, J. M.; Sicklinger, J.; Döblinger, M.; Böcklein, S.; Ziegler, J.; Peter, L.; Rathousky, J.; Scheidt, E.-W.; Bein, T.; Fattakhova-Rohlfing, D. *Adv. Funct. Mater.* **2014**, *24*, 3123.
(2) Wang, J.; Li, K.; Zhong, H.-x.; Xu, D.; Wang, Z.-l.; Jiang, Z.; Wu, Z.-j.; Zhang, X.-b. *Angew. Chem., Int. Ed.* **2015**, *54*, 10530.
(3) Miller, E. L.; Rocheleau, R. E. *J. Electrochem. Soc.* **1997**, *144*, 1995.
(4) Miller, E. L.; Rocheleau, R. E. *J. Electrochem. Soc.* **1997**, *144*, 3072.
(5) Trotochaud, L.; Young, S. L.; Ranney, J. K.; Boettcher, S. W. *J. Am. Chem. Soc.* **2014**, *136*, 6744.
(6) Zhu, Y.; Cao, C.; Tao, S.; Chu, W.; Wu, Z.; Li, Y. *Sci. Rep.* **2014**, *4*, 5787.
(7) Fominykh, K.; Chernev, P.; Zaharieva, I.; Sicklinger, J.; Stefanic, G.; Doeblinger, M.; Mueller, A.; Pokharel, A.; Boecklein, S.; Scheu, C.; Bein, T.; Fattakhova-Rohlfing, D. *ACS Nano* **2015**, *9*, 5180.
(8) Trotochaud, L.; Ranney, J. K.; Williams, K. N.; Boettcher, S. W. *J. Am. Chem. Soc.* **2012**, *134*, 17253.
(9) Shu, X.; An, Z.; Wang, L. Y.; He, J. *Chem. Commun.* **2009**, 5901.
(10) Gao, M. R.; Sheng, W. C.; Zhuang, Z. B.; Fang, Q. R.; Gu, S.; Jiang, J.; Yan, Y. S. *J. Am. Chem. Soc.* **2014**, *136*, 7077.
(11) Patra, A. K.; Kundu, S. K.; Kim, D.; Bhaumik, A. *ChemCatChem* **2015**, *7*, 791.
(12) Duan, H.; Yan, N.; Yu, R.; Chang, C. R.; Zhou, G.; Hu, H. S.; Rong, H.; Niu, Z.; Mao, J.; Asakura, H.; Tanaka, T.; Dyson, P. J.; Li, J.; Li, Y. *Nat. Commun.* **2014**, *5*, 3093.
(13) Tan, C. L.; Qi, X. Y.; Huang, X.; Yang, J.; Zheng, B.; An, Z. F.; Chen, R. F.; Wei, J.; Tang, B. Z.; Huang, W.; Zhang, H. *Adv. Mater.* **2014**, *26*, 1735.
(14) Sun, Y. F.; Liu, Q. H.; Gao, S.; Cheng, H.; Lei, F. C.; Sun, Z. H.; Jiang, Y.; Su, H. B.; Wei, S. Q.; Xie, Y. *Nat. Commun.* **2013**, *4*, 2899.
(15) Zhang, X.; Lai, Z.; Liu, Z.; Tan, C.; Huang, Y.; Li, B.; Zhao, M.; Xie, L.; Huang, W.; Zhang, H. *Angew. Chem., Int. Ed.* **2015**, *54*, 5425.
(16) Su, D.; Ford, M.; Wang, G. *Sci. Rep.* **2012**, *2*, 924.
(17) Feng, L.-L.; Yu, G.; Wu, Y.; Li, G.-D.; Li, H.; Sun, Y.; Asefa, T.; Chen, W.; Zou, X. *J. Am. Chem. Soc.* **2015**, *137*, 14023.
(18) Friebel, D.; Louie, M. W.; Bajdich, M.; Sanwald, K. E.; Cai, Y.; Wise, A. M.; Cheng, M.-J.; Sokaras, D.; Weng, T.-C.; Alonso-Mori, R.; Davis, R. C.; Bargar, J. R.; Nørskov, J. K.; Nilsson, A.; Bell, A. T. *J. Am. Chem. Soc.* **2015**, *137*, 1305.
(19) Li, H.; Tsai, C.; Koh, A. L.; Cai, L.; Contryman, A. W.; Fragapane, A. H.; Zhao, J.; Han, H. S.; Manoharan, H. C.; Abild-Pedersen, F.; Norskov, J. K.; Zheng, X. *Nat. Mater.* **2016**, *15*, 48.
(20) Suntivich, J.; May, K. J.; Gasteiger, H. A.; Goodenough, J. B.; Shao-Horn, Y. *Science* **2011**, *334*, 1383.
(21) Hong, W. T.; Risch, M.; Stoerzinger, K. A.; Grimaud, A.; Suntivich, J.; Shao-Horn, Y. *Energy Environ. Sci.* **2015**, *8*, 1404.
(22) Liu, Y.; Xiao, C.; Lyu, M.; Lin, Y.; Cai, W.; Huang, P.; Tong, W.; Zou, Y.; Xie, Y. *Angew. Chem., Int. Ed.* **2015**, *54*, 11231.
(23) Moniz, S. J. A.; Shevlin, S. A.; Martin, D. J.; Guo, Z.-X.; Tang, J. *Energy Environ. Sci.* **2015**, *8*, 731.
(24) Gong, M.; Zhou, W.; Tsai, M.-C.; Zhou, J.; Guan, M.; Lin, M.-C.; Zhang, B.; Hu, Y.; Wang, D.-Y.; Yang, J.; Pennycook, S. J.; Hwang, B.-J.; Dai, H. *Nat. Commun.* **2014**, *5*, 4695.
(25) Hu, H.; Guan, B.; Xia, B.; Lou, X. W. *J. Am. Chem. Soc.* **2015**, *137*, 5590.
(26) Yang, Y.; Sun, C.; Wang, L.; Liu, Z.; Liu, G.; Ma, X.; Cheng, H.-M. *Adv. Energy Mater.* **2014**, *4*, 1400057.
(27) Wang, Q.; O'Hare, D. *Chem. Rev.* **2012**, *112*, 4124.
(28) Ma, R.; Sasaki, T. *Adv. Mater.* **2010**, *22*, 5082.
(29) Zhao, Y.; Li, B.; Wang, Q.; Gao, W.; Wang, C. J.; Wei, M.; Evans, D. G.; Duan, X.; O'Hare, D. *Chem. Sci.* **2014**, *5*, 951.
(30) Shao, M.; Ning, F.; Zhao, J.; Wei, M.; Evans, D. G.; Duan, X. *J. Am. Chem. Soc.* **2012**, *134*, 1071.
(31) Fan, G.; Li, F.; Evans, D. G.; Duan, X. *Chem. Soc. Rev.* **2014**, *43*, 7040.
(32) Zhao, Y. F.; Wang, Q.; Bian, T.; Yu, H. J.; Fan, H.; Zhou, C.; Wu, L. Z.; Tung, C. H.; O'Hare, D.; Zhang, T. R. *Nanoscale* **2015**, *7*, 7168.
(33) Shu, X.; He, J.; Chen, D.; Wang, Y. *J. Phys. Chem. C* **2008**, *112*, 4151.
(34) Liu, G.; Yang, H. G.; Wang, X.; Cheng, L.; Pan, J.; Lu, G. Q.; Cheng, H.-M. *J. Am. Chem. Soc.* **2009**, *131*, 12868.
(35) He, S.; Zhang, S.; Lu, J.; Zhao, Y.; Ma, J.; Wei, M.; Evans, D. G.; Duan, X. *Chem. Commun.* **2011**, *47*, 10797.
(36) Zhao, J.; Chen, J.; Xu, S.; Shao, M.; Zhang, Q.; Wei, F.; Ma, J.; Wei, M.; Evans, D. G.; Duan, X. *Adv. Funct. Mater.* **2014**, *24*, 2938.
(37) Anspoks, A.; Kalinko, A.; Kalendarev, R.; Kuzmin, A. *Phys. Rev. B: Condens. Matter Mater. Phys.* **2012**, *86*, 174114.
(38) Sun, Y.; Gao, S.; Lei, F.; Xiao, C.; Xie, Y. *Acc. Chem. Res.* **2015**, *48*, 3.
(39) Stoyanova, R.; Zhecheva, E.; Alcantara, R.; Tirado, J. L. *J. Phys. Chem. B* **2004**, *108*, 4053.
(40) Davidson, A.; Tempere, J. F.; Che, M.; Roulet, H.; Dufour, G. *J. Phys. Chem.* **1996**, *100*, 4919.
(41) Sasi, B.; Gopchandran, K. G. *Nanotechnology* **2007**, *18*, 115613.
(42) Man, I. C.; Su, H.-Y.; Calle-Vallejo, F.; Hansen, H. A.; Martinez, J. I.; Inoglu, N. G.; Kitchin, J.; Jaramillo, T. F.; Norskov, J. K.; Rossmeisl, J. *ChemCatChem* **2011**, *3*, 1159.
(43) Viswanathan, V.; Hansen, H. A.; Rossmeisl, J.; Norskov, J. K. *ACS Catal.* **2012**, *2*, 1654.
(44) Liu, Y.; Cheng, H.; Lyu, M.; Fan, S.; Liu, Q.; Zhang, W.; Zhi, Y.; Wang, C.; Xiao, C.; Wei, S.; Ye, B.; Xie, Y. *J. Am. Chem. Soc.* **2014**, *136*, 15670.
(45) Lu, X.; Wang, G.; Zhai, T.; Yu, M.; Gan, J.; Tong, Y.; Li, Y. *Nano Lett.* **2012**, *12*, 1690.
(46) Nowotny, M. K.; Sheppard, L. R.; Bak, T.; Nowotny, J. *J. Phys. Chem. C* **2008**, *112*, 5275.
(47) Chen, J.; Song, W.; Hou, H.; Zhang, Y.; Jing, M.; Jia, X.; Ji, X. *Adv. Funct. Mater.* **2015**, *25*, 6793.
(48) Cho, I. S.; Logar, M.; Lee, C. H.; Cai, L.; Prinz, F. B.; Zheng, X. *Nano Lett.* **2014**, *14*, 24.
(49) Rahman, M. A.; Bazargan, S.; Srivastava, S.; Wang, X.; Abd-Ellah, M.; Thomas, J. P.; Heinig, N. F.; Pradhan, D.; Leung, K. T. *Energy Environ. Sci.* **2015**, *8*, 3363.
(50) Tang, C.; Cheng, N.; Pu, Z.; Xing, W.; Sun, X. *Angew. Chem., Int. Ed.* **2015**, *54*, 9351.
(51) Gu, Y. H.; Lu, Z. Y.; Chang, Z.; Liu, J. F.; Lei, X. D.; Li, Y. P.; Sun, X. M. *J. Mater. Chem. A* **2013**, *1*, 10655.
(52) Li, Y.-F.; Liu, Z.-P. *J. Am. Chem. Soc.* **2011**, *133*, 15743.
(53) Lu, Z.; Zhu, W.; Yu, X.; Zhang, H.; Li, Y.; Sun, X.; Wang, X.; Wang, H.; Wang, J.; Luo, J.; Lei, X.; Jiang, L. *Adv. Mater.* **2014**, *26*, 2683.
(54) Amano, F.; Nakata, M.; Yamamoto, A.; Tanaka, T. *J. Phys. Chem. C* **2016**, *120*, 6467.
(55) Zhao, Y. F.; Chen, P.; Zhang, B.; Su, D. S.; Zhang, S.; Tian, L.; Lu, J.; Li, Z.; Cao, X.; Wang, B.; Wei, M.; Evans, D. G.; Duan, X. *Chem. - Eur. J.* **2012**, *18*, 11949.
(56) Gong, M.; Li, Y. G.; Wang, H. L.; Liang, Y. Y.; Wu, J. Z.; Zhou, J. G.; Wang, J.; Regier, T.; Wei, F.; Dai, H. J. *J. Am. Chem. Soc.* **2013**, *135*, 8452.
(57) Zhao, Y.; Zhang, S.; Li, B.; Yan, H.; He, S.; Tian, L.; Shi, W.; Ma, J.; Wei, M.; Evans, D. G.; Duan, X. *Chem. - Eur. J.* **2011**, *17*, 13175.

DOI: 10.1021/jacs.6b01606
J. Am. Chem. Soc. 2016, 138, 6517−6524